PHYSICAL REVIEW E **113**, 065413 (2026)

Dispersion relations for active undulators in overdamped environments

Christopher J. Pierce,[1,2] Daniel Irvine,[3] Lucinda Peng,[2] Xuefei Lu,[2] Hang Lu,[2] and Daniel I. Goldman[1]
[1]*School of Physics, Georgia Institute of Technology, Atlanta, Georgia 30332, USA*
[2]*School of Chemical and Biomolecular Engineering, Georgia Institute of Technology, Atlanta, Georgia 30332, USA*
[3]*Department of Mathematics, Kennesaw State University, Kennesaw, Georgia 30144, USA*

(Received 17 July 2024; accepted 6 May 2026; published 15 June 2026)

Organisms that locomote by propagating approximately sinusoidal waves of body bending maintain performance across different environmental substrates by modifying the frequency ω or wave number k of their gait. We identify a unifying relationship between these parameters for overdamped undulatory swimmers (including nematodes, spermatozoa, and mm-scale fish) moving in diverse environmental rheologies, in the form of an active "dispersion relation" $\omega \propto k^{\pm 2}$. A model treating the organisms as actively driven viscoelastic beams in a surrounding fluid reproduces the experimentally observed scaling. The relative strength of rate-dependent dissipation in the body and in the environment determines whether k^{-2} or k^2 scaling is observed. The existence of these scaling regimes reflects the k and ω dependence of the various underlying force terms and how their relative importance changes with the composition of the external environment and the parameters of neuronally commanded gait. In the regime where the body dissipation dominates, the application of boundary conditions does not introduce an explicit dependence on the body length, as would be expected in other wave systems in physics. Hence, mechanics constrains the relationship between the gait parameters but allows for their continuous variation along the dispersion curve.

DOI: 10.1103/lszs-51bf

I. INTRODUCTION

Organismal self-propulsion results from the cyclical self-deformation of a body in space and time. In overdamped mechanical regimes, these self-deformations, or gaits, produce center-of-mass displacements that are independent of the period of the gait, due to the dominance of dissipation over inertia [1]. Once thought to be restricted to the microscopic domain of low Reynolds number swimming in water and complex biofluids, subsequent work has revealed that many terrestrial locomotor systems, such as snakes [2] and centipedes [3], also operate in overdamped regimes where inertia, and hence coasting (defined as the ratio of the time taken to stop after cessation of activity to the cycle duration) is negligible [4,5]. Principles of locomotion in overdamped regimes can therefore help to describe organisms across scales, environments, and taxa [6].

Because the displacement is rate independent, theoretical models of low-coasting locomotion (e.g., resistive-force theory [7,8], slender-body theory [9], geometric mechanics [4,10]) often describe relationships between spatial variables. On the other hand, temporal parameters, such as the frequency of undulation ω, are nonetheless important; they affect the energetics of locomotion, and organisms operate under power constraints. Understanding why organisms in overdamped regimes select particular gaits requires consideration of the tradeoffs between optimal kinematics and power constraints [11]. These tradeoffs indirectly couple the spatial and temporal parameters of the gait.

Here, we identify a link between the temporal and spatial traveling wave dynamics of undulatory gaits in the form of a functional relationship between the wave number k and frequency ω. We first observed this relationship in an experimental study of nematode locomotion in a variety of complex environments. We explain our observations by deriving an active "dispersion relation" $\omega(k)$ from force balance, assuming a muscle torque in the form of a traveling wave phase shifted with respect to the body-bending wave [12–14]. This dispersion relation holds not only for worms moving through a broad range of rheologies, but also for a set of unrelated undulatory systems (spermatozoa and fish larvae). Unlike many other wave systems within physics, the application of boundary conditions to the model does not introduce a length-dependent restriction on the possible values of k. This explains the experimental observation that nematodes continuously vary their gait parameters depending on the composition of their environment, producing a continuous spectrum of gaits.

II. RESULTS

A. Measuring k and ω

We first describe a systematic experimental study of the forward swimming gaits of the nematode *Caenorhabditis elegans*. *C. elegans* encounters diverse environments in its native habitat [18] and can locomote in a variety of complex laboratory environments via dorsoventral bends that pass from head to tail [19–22]. This species modifies its gait parameters as a function of environmental viscosity to maintain gait performance [16]. See Fig. 1. We experimentally measured ω and k [23] for *C. elegans* in a diverse set of environments including buffer solutions, methylcellulose mixtures of different viscosities (weakly viscoelastic fluids), polyethylene glycol (PEG) hydrogels with a range of bulk moduli, and agar surfaces. (See the Supplemental Material [17] for details.) We also compared

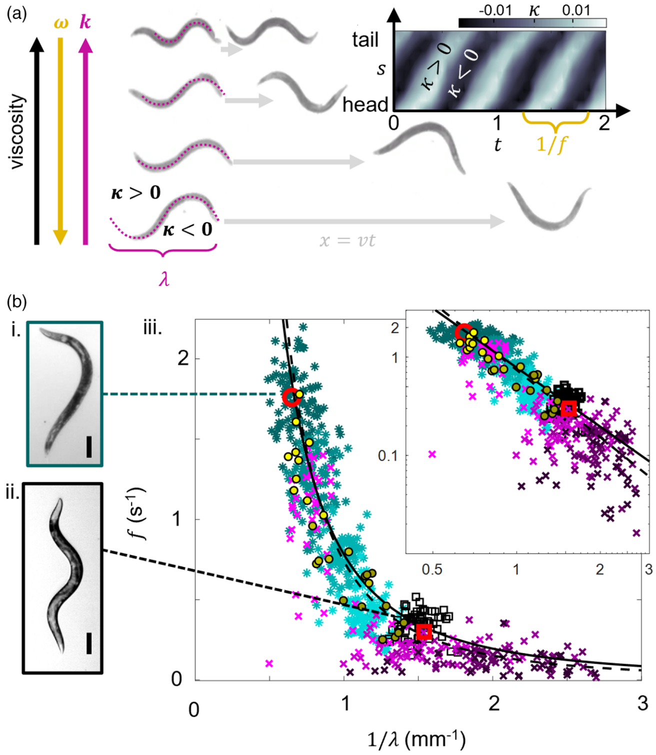

FIG. 1. Dispersion relation showing the approximate inverse quadratic scaling of $\omega \propto f$ with $k \propto 1/\lambda$ for *C. elegans* under changing environmental rheology. (a) Brightfield images of worm body shapes traveling through fluids of different viscosities, final positions are after 4.5 s elapsed time. Violet curves illustrate full wave periods to show the changing wavelength λ. Inset, heatmap showing curvature κ (in units of mm^{-1}) along the body coordinate s (the arc length from head to tail in units of body length) and through time (in seconds) showing alternating bands of positive and negative curvature oscillating at a frequency f. (b) Postures of nematodes in buffer (part i) and agar (part ii) (scale bar, 1 mm). Linear (part iii) and log plot (inset of iii) of the experimental dispersion relation for nematodes in diverse environments shown with the inverse quadratic (solid black line) and power-law (dashed black line) fits, along with experimental data ∗ methylcellulose (0–3%), □ Agar, × PEG (1–5%), ● dextran from Butler *et al.* [15], ○ buffer and □ agar from Fang-yen *et al.* [16]. Power-law exponent is -2.28 ± 0.30. See Supplemental Material [17] for an expanded version of this plot and full legend.

our measured gaits to two literature sources, including previously measured buffer-swimming and agar-crawling gaits [16], and swimming gaits in dextran mixtures with various viscosities [15], which remain Newtonian over a broad range of concentrations.

Surprisingly, across these diverse rheologies, *C. elegans'* gaits fall approximately on a single curve given by the dispersion relation $\omega(k) \propto k^{-2}$. Figure 1(b) shows the data along with a fit to an inverse quadratic function (solid line, $R^2 = 0.98$) and a power-law fit (dashed line, $R^2 = 0.99$), which yielded an exponent of -2.28 ± 0.30.

B. Modeling force balance

To explain this observation, we constructed a mechanical model based on force balance. We consider a driven viscoelastic (Kelvin-Voight) beam previously used to model terrestrial undulation of snakes on frictional surfaces (where friction dominates inertia) [24]. This model was subsequently used to describe nematodes immersed in a low Reynolds-number fluid [16].

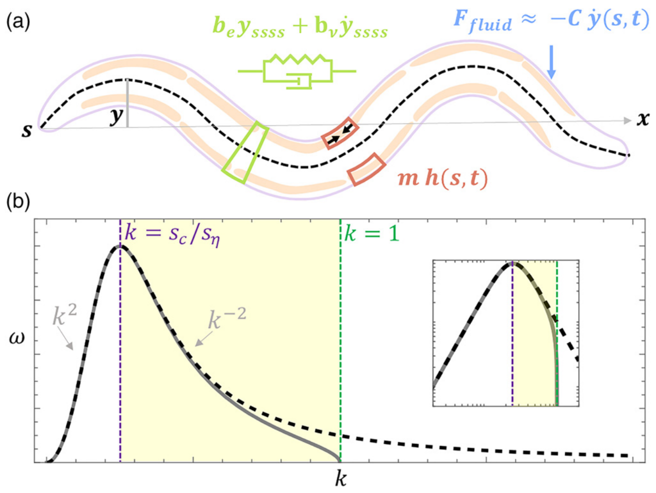

FIG. 2. An active damped beam model and resulting dispersion relations. (a) Model variables and internal and external forces for a generic undulator in a fluid. (b) The real part of the full dispersion relation (dashed, black curve) and the real part of the dispersion curve with the constraint of wave stability imposed (solid, gray curve). (b) Inset: The same curves on a log-log scale. Dashed vertical lines indicate the value of k separating quadratic and inverse scaling (purple) and the wave stability cutoff (green), for $x_c/x_\eta = 0.25$. The yellow shaded region shows the domain in k which applies to the locomotion of *C. elegans*.

We next consider the balance of the linear force density along the body, by equating the forces derived from the internal moments of the beam (collectively called M) to the external resistive forces from the fluid (F_{fluid}). We assume that both M and F_{fluid} are functions of the arclength s along the beam and of time t. In the following analysis we make the approximation $s \approx x$ [see Fig. 2(a)]. Balance of force density gives

$$M_{xx}(x,t) = F_{\text{fluid}}(x,t). \tag{1}$$

In this equation, the variable x in the subscript denotes partial derivative with respect to x. In Eq. (1) we include three internal moments associated with the body elasticity, rate-dependent damping in the body, and an active moment associated with the muscles. For the fluid drag, we use a resistive-force model. Substituting these particular force terms into Eq. (1), we arrive at the following partial differential equation

$$b_e y_{xxxx} + b_\eta \frac{\partial}{\partial t} y_{xxxx} + m h_{xx} = -C \frac{\partial y}{\partial t}. \tag{2}$$

Here $y(x,t)$ is the lateral displacement of the beam. The passive internal force densities are $b_e y_{xxxx}$ for the body elasticity, $b_\eta \frac{\partial}{\partial t} y_{xxxx}$ for the rate-dependent body damping. Here $m h_{xx}$ is the force density from the active moment produced by the muscles, which we have written in terms of a constant m with units of torque, and a dimensionless function $h(x,t)$, which describes the spatiotemporal variation of the driving torque. The external viscous fluid drag in the y direction is given as $-C\frac{\partial y}{\partial t}$ [25].

This force balance equation (2) implies two characteristic length scales and a single characteristic time scale. (See the Supplemental Material [17] for a derivation.) Here we have chosen to scale the lengths y and x by the length scale $x_c = b_e/m$, which represents the minimal radius of curvature achieved by the body when the muscle torque m is balanced entirely by the body elasticity; we scale time by $t_c = b_\eta/b_e$, which represents the viscoelastic relaxation time of the passive body (see Supplemental Material [17] for further discussion).

The second length scale implied by Eq. (2), $x_\eta = (\frac{b_\eta}{C})^{1/4}$, relates to the relative strength of internal and external dissipation terms $b_\eta \frac{\partial}{\partial t} y_{xxxx}$ and $C\frac{\partial y}{\partial t}$. Specifically, $\lambda = x_\eta$ is the undulation wavelength at which the two dissipative terms are equal in magnitude. While we have not chosen to scale the equation of motion using x_η, it remains important in characterizing the dynamics, as shown below.

Using x_c and t_c, we produce the following dimensionless equation of motion:

$$\upsilon_{\sigma\sigma\sigma\sigma} + \dot{\upsilon}_{\sigma\sigma\sigma\sigma} + h_{\sigma\sigma} = -\left(\frac{x_c}{x_\eta}\right)^4 \dot{\upsilon}. \tag{3}$$

Here υ represents the nondimensional variable that corresponds to y. The dimensionless independent variables σ and τ correspond to x and t, respectively. The overdot represents partial differentiation with respect to τ. The function $h(\sigma, \tau)$ represents the spatiotemporal variation in the muscle torque, as above, but as a function of the new dimensionless variables.

We solve Eq. (3) by substituting a right-traveling plane-wave ansatz solution

$$\upsilon(\sigma, \tau) = \exp(i(k\sigma - \omega\tau)),$$

with wave number k and angular frequency ω, and by specifying a particular form of the muscle torque function h. We make this substitution with the expectation that the real part of the solution will describe the emergent oscillations in worms. Previous measurements in fish, lizards, and nematodes showed that muscle activity patterns are approximately sinusoidal and are temporally phase shifted relative to the body bends [12–14]. This phenomenon is referred to as a *neuromechanical phase lag*. These phase lags arise generically in elongated swimmers because the muscle at a given point must balance both local and nonlocal torques [13]. These experimental observations allow us to write an empirical muscle forcing term (without making reference to any model of the neuronal control) in the form of plane wave that is phase shifted relative to our ansatz solution $\upsilon(\sigma, \tau)$,

$$h = e^{-i\phi} \cdot \upsilon. \tag{4}$$

Here $\phi > 0$ represents a phase lag relative to the body bending waves. (See the Supplemental Material [17] for sign conventions.) Finally, we solve for ω to produce the dispersion relation with real and imaginary parts:

$$\mathrm{Re}\{\omega(k)\} = \frac{k^2 \sin(\phi)}{(x_c/x_\eta)^4 + k^4}, \tag{5}$$

and

$$\mathrm{Im}\{\omega(k)\} = \frac{k^2 \cos(\phi) - k^4}{(x_c/x_\eta)^4 + k^4}. \tag{6}$$

The oscillation of a solution to Eq. (2) is governed by the real part of the dispersion relation (5), which is plotted in Fig. 2(b) as a dashed curve. For oscillations to persist in time, the imaginary part (6) must vanish. Setting Eq. (6) to zero, we establish the following criterion for wave stability:

$$k^2 = \cos\phi. \tag{7}$$

We enforce this criterion by substituting Eq. (7) into Eq. (5), yielding

$$\mathrm{Re}\{\omega(k)\} = \frac{k^2\sqrt{1-k^4}}{(x_c/x_\eta)^4 + k^4}, \tag{8}$$

which introduces an additional factor of $\sqrt{1-k^4}$ to Eq. (5). This modified dispersion curve is shown in Fig. 2(b) as a solid, gray curve. The stability criterion places a constraint, $k < 1$, on the possible values of the dimensionless wave number. Because of our choice of nondimensionalization, this is equivalent to the condition that the wavelength be greater than the characteristic length scale $\lambda > 2\pi x_c$ (in natural units).

C. Inverse quadratic scaling in the model

We now consider the following question. For what range of wave numbers will the dispersion relation (8) support an inverse quadratic scaling? For $k < x_c/x_\eta$, the dispersion relation scales approximately *quadratically* [Fig. 2(b)]. Alternatively, in the domain $k > x_c/x_\eta$ and $k < 1$, we recover the experimentally observed relationship $\omega \propto k^{-2}$. This implies that k^{-2} can only be observed when the wavelength $\lambda/2\pi$, taken in natural units, is less than x_η, but greater than x_c. This, in turn, suggests that nematodes operate in a regime where the largest source of dissipation is within the body's bending degree of freedom, and not from the surrounding fluid, since $\lambda < 2\pi x_\eta$ is the regime where internal dissipation exceeds external viscous dissipation forces. This finding suggests that internal damping within the body plays a more significant role in nematode biomechanics than previously thought [16].

To model this internal dissipation-dominated regime, we therefore eliminate the viscous drag term in Eq. (3), producing a simplified equation of motion:

$$\upsilon_{\sigma\sigma\sigma\sigma} + \dot{\upsilon}_{\sigma\sigma\sigma\sigma} + h_{\sigma\sigma} = 0. \tag{9}$$

Calculating the dispersion relation for this regime, we recover the same stability criterion described above (7). Substituting into the real part of the dispersion relation for the internal dissipation regime, we obtain

$$\mathrm{Re}\{\omega(k)\} = \frac{\sqrt{1-k^4}}{k^2}. \tag{10}$$

By restoring units, we can determine the constant of proportionality (to leading order)

$$f = \frac{\lambda^2}{2\pi t_c x_c^2} = \alpha\lambda^2. \tag{11}$$

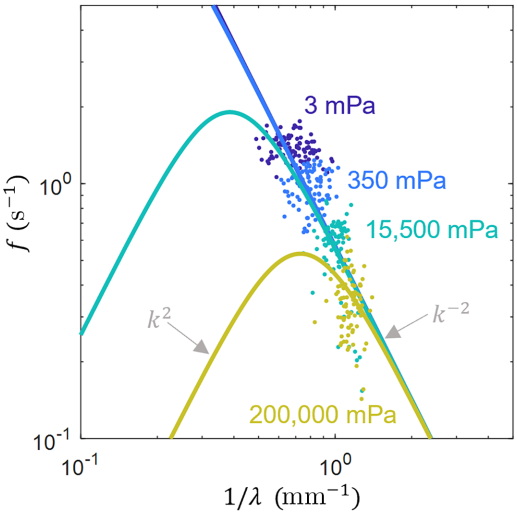

FIG. 3. Dispersion relation (5) in natural units for different values of fluid drag coefficient C taken from methylcellulose data. All the *C. elegans* data lie in the $k > x_c/x_\eta$ regime and are insensitive to the precise location of the peak at $k = x_c/x_\eta$.

Here, we have defined the constant $\alpha = (2\pi t_c x_c^2)^{-1} = m^2/(2\pi b_\eta b_e)$. From a fit to the data in Fig. 1(a), we estimate the value of the proportionality constant to be $\alpha = 0.69 \pm 0.02$ s^{-1} mm^{-2}.

D. Dependence on model parameters

Having identified the origin of inverse quadratic scaling in the dispersion relation, we next discuss how the model parameters change with the composition of the external environment by returning to our experimental data. For the nematodes to obey a constant scaling relationship across individuals and across the various experimental environments, α must be constant. The lack of dependence on C in Eq. (10) suggests that viscosity shifts will not alter the scaling, but only change the location of the maximum value separating the k^2 and k^{-2} regimes, because x_η (and hence the value of k that separates the two regimes) does depend on viscosity. Restoring units to the model using measured viscosities and comparing with the methylcellulose data, Fig. 3 shows that, indeed, while the viscosity affects the relative distance of the experimental wave numbers to the peak of the dispersion curve, it does not change the overall k^{-2} relationship. Increasing the viscosity does, however, induce the worm to select a different ω as previously noted [16], producing the observed gait spectrum (Fig. 1).

We next consider changes in the *elasticity* of the surrounding medium. For example, in the PEG hydrogel experiments [magenta points in Fig. 1(b)], nematodes encounter a highly elastic environment relative to methylcellulose, dextran, and buffer solutions. In these data, the scaling persists because the addition of a linear elastic term to Eq. (3) does not impact the scaling of the real part of the dispersion (5), and only adds a constant offset to the numerator in Eq. (6). Hence, environmental elasticity will change the stability criterion, but does not impact the scaling of the real part of the dispersion for values of k that maintain stability.

E. The effect of the boundary

To model the effect of the boundary on the gait spectrum, we apply force- and moment-free boundary conditions [26,27] to the nondimensionalized solutions in the k^{-2} regime described by Eq. (9). These boundary conditions require the internal forces and moments to go to zero at either end of the organism, i.e., at $\sigma = 0$ and $\sigma = L/x_c$. (Because these forces and moments are internal to the organism's body, they must vanish at the endpoints.) The moment-free boundary condition is

$$M = \upsilon_{\sigma\sigma} + \dot{\upsilon}_{\sigma\sigma} + e^{-i\phi}\upsilon = 0. \tag{12}$$

Substituting the right-traveling wave ansatz, we may write

$$[-k^2 - i\omega k^2 + e^{i\phi}]\,\upsilon(\sigma, \tau) = 0 \tag{13}$$

which is satisfied for all σ, τ if

$$\mathrm{Re}\{\omega(k)\} = \frac{\sin\phi}{k^2}\mathrm{Im}\{\omega(k)\} = \frac{\cos\phi}{k^2} - 1. \tag{14}$$

If we apply the stability criterion $Im\{\omega(k)\} = 0$ and substitute the result into the real part of Eq. (14), we produce the same dispersion relation acquired from force density balance in the internal dissipation regime (10).

Similarly, the force-free boundary condition is

$$F_{\mathrm{int}} = M_\sigma = \upsilon_{\sigma\sigma\sigma} + \dot{\upsilon}_{\sigma\sigma\sigma} + e^{i\phi}\upsilon = 0. \tag{15}$$

We again substitute the right-traveling wave ansatz, and we use Eq. (13) to find

$$M_\sigma = [-ik^3 + \omega k^3 + ike^{-i\phi}]\upsilon(\sigma, \tau) = \tag{16}$$

$$ik[-k^2 - i\omega + e^{-i\phi}]\upsilon(\sigma, \tau) = 0, \tag{17}$$

$$ikM = 0. \tag{18}$$

This condition is also satisfied by a solution with an identical dispersion relation.

Recapitulating, the ansatz solution that satisfies the equation of motion in the internal dissipation regime (9) also satisfies the moment- and force-free boundary conditions at *all points along the body*, including the ends. Therefore, the finite size of the organism does not constrain the solutions. This situation arises as a consequence of the relationship between the boundary conditions and Eq. (9). In situations where the force balance is governed by internal moments, *and where inertia may be ignored*, the effect of the free boundaries may be neglected. For an analysis of the boundary conditions applied to the full equation of motion (3), including the external drag, see Appendix A.

F. Experimental evidence for k^2 scaling

In the regime where $k < x_c/x_\eta$ and $k < 1$, Eq. (8) scales approximately as $\omega \propto k^2$ and the dominant dissipation term is the external viscous dissipation. We may recover this scaling by eliminating the internal dissipation term from Eq. (3), which yields the following equation of motion

$$\upsilon_{\sigma\sigma\sigma\sigma} + h_{\sigma\sigma} = -\left(\frac{x_c}{x_\eta}\right)^4 \dot{\upsilon}, \tag{19}$$

and the corresponding dispersion relation

$$\mathrm{Re}\{\omega(k)\} = \frac{x_\eta^2}{x_c^2} k^2 \sqrt{1-k^4}, \tag{20}$$

after enforcing the stability criterion [28]. Restoring units, we find, to leading order,

$$f = \frac{2\pi x_\eta^2}{t_c \lambda^2} = \frac{\beta}{\lambda^2}, \tag{21}$$

where we have defined $\beta = 2\pi x_\eta^2/t_c = 2\pi b_e (b_\eta C)^{-1/2}$.

We next asked if there was any experimental evidence for the existence of a k^2 regime. We considered several literature sources of gait parameters measured in other undulators, a meta-analysis of fish swimming [29], the bank of swimming organisms at the micron scale (BOSO-Micro) database [30], where we investigated the gaits of spermatozoa, an analysis of other nematode species' gaits [31], and a study of polychaete worms in water and sediment [32]. The non-*C. elegans* nematodes and polychaete worms displayed frequencies that *decreased* with k across environments. (The data was insufficient to evaluate the scaling, however.) In contrast, for both the spermatozoa and the fish data, ω *increased* with k, suggesting that they may operate in the external dissipation-dominated regime implied by our model.

For many fish, the body and fluid dynamics are inertial. Unsurprisingly, the majority of the data in the meta-analysis [29] do not fit well to a k^2 model, which assumes that inertia is negligible. A small number of organisms, however, with Reynolds numbers (Re) under 2000 and Strouhal numbers (St) greater than 0.7, approximately fit to a k^2 dispersion relation [see Fig. 4(a)]. We note that while Re ∼2000 is inertial, the drag coefficient remains approximately linear in velocity at intermediate Reynolds numbers (See, for example, Ref. [36], Ch. 14). Furthermore, Ref. [29] noted the existence of two distinct swimming regimes based on the same criteria. Unsurprisingly, organisms in this regime were some of the smallest species in the study, and with one exception were collected from different larval stages [see Fig. 4(a)]. We estimate the proportionality constant in Eq. (21) to be $\beta_{Fish} = 9.4 \pm 1.0\ \mathrm{s}^{-1}\,\mathrm{m}^2$.

We also fit the spread of the spermatozoa data to a k^2 relationship and find a rough agreement, with a constant of $\beta_{Sp.} = (8 \pm 3) \times 10^{-3}\ \mathrm{s}^{-1}\,\mathrm{mm}^2$. Cricket sperm are particularly interesting in terms of their dispersion relations, because their unusually long flagella (≈ mm) exhibit spatial variation in k and ω [35]. Thus, an individual cell's flagellum allows a test of the model where the biomechanical parameters are likely held constant. Figure 4(d) shows cricket sperm data from Ref. [35] along with a fit yielding a constant of $\beta_{Crick.} = (7 \pm 4) \times 10^{-5}\ \mathrm{s}^{-1}\,\mathrm{mm}^2$. Finally, see the Supplemental Material [17] for a linear plot of the data in Fig. 4.

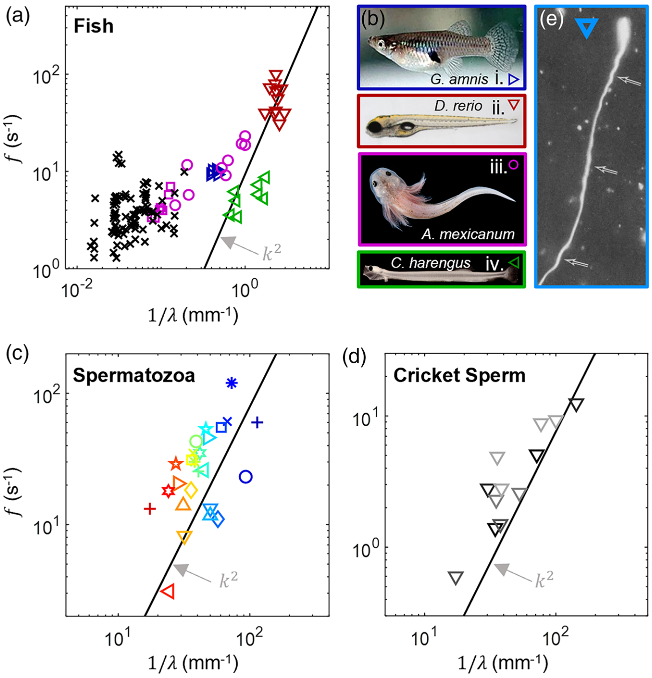

FIG. 4. Fish larvae and spermatozoa display dispersion relations where f is an increasing function of $1/\lambda$, indicating that external fluid dissipation dominates internal dissipation. (a) Data from fish-swimming meta-analysis with selected low-inertia swimmers separated by species (high-inertia swimmers plotted in black). Images of a mosquitofish *G. amnis* (∼cm, Wikipedia) (b)(part i), zebrafish larva, *D. rerio* (∼mm, from Ref. [33]) (b)(part ii), an axolotl larva *A. mexicanum* (∼cm, photo credit John P. Clare) (b)(part iii), and a herring larva *C. harengus* (∼mm, from Ref. [34]) (b)(part vi). (c) Spermatozoa data from different species taken from Ref. [30] along with quadratic fit, + *P. maxima* (turbot), ○ *A. curtula* (beetle), ∗ *Lygaeus* (milkweed bug), × *T. thynnus* (tuna), □ *M. merluccius* (hake), ◇ *C. capitata* (fly), ▽ cricket, △ *B. marinus* (toad), ▷ *Colobocentrotus* (sea urchin), ★ *G. morhua* (cod), ◁ *Chaetopterus* (annelid), ✡ *Psammechinus* (sea urchin), + *G. domesticus* (domestic fowl), ○ *Ostrea* (oyster), ∗ *Lytechinus* (sea urchin), × *Ciona* (tunicate), □ *S. purpuratus* (sea urchin), ◇ *Myzostomus* (worm), ▽ *C. mellus* (midge), △ *Homo* (human), ▷ *Bos*, bull, ★ *Ovis* (ram), ◁ *M. sclaris* (fly), ✡ rabbit, + *Mus* (mouse), (d) Cricket sperm dispersion relation for multiple individuals with multiple measurements along each flagellum from Ref. [35] (different gray values represent different individuals), along with (e) an image of multiple waves on a single cricket flagellum (∼0.1–1mm) [35].

III. CONCLUSION

In this work, we found that the undulatory gait parameters of the nematode *C. elegans*, across a wide range of environments, accumulate around a single curve given by $\omega \propto k^{-2}$. To explain this observation, we constructed a neuromechanical model treating the undulator as an active viscoelastic beam in a fluid. We then analyzed the partial differential that arises from force balance. Based on our prior measurements of muscle activity in *C. elegans* [14] and similar phenomena in vertebrates [12,13], we modeled the active forces from the muscles as a traveling wave of force, phase shifted relative to the traveling wave of body bends. Our model recapitulated the observed k^{-2} dispersion for a range of parameters, and also predicted the existence of a k^2 regime. We found preliminary evidence for the quadratic regime from existing data in the literature describing the gaits of a diverse set of fish larvae and spermatozoa. Surprisingly, unlike many other wave systems in physics, we observed no evidence of discretization in the spectrum of gaits, despite the finite length of the undulator.

Our model explains why, in this particular system, the effect of the boundaries does not introduce a length-dependent discretization condition. In the internal dissipation-dominant regime, the boundary conditions are trivially satisfied by any solution that also satisfies the force balance enforced at all points along the length of the undulator. Thus, our model explains how the organism may continuously vary ω (or k) as observed.

Because ω and k are functionally related, selecting one variable determines the other. However, our mechanical model does not explain how an individual undulator's locomotor control system selects a particular point along this curve. For nematodes, based on models of proprioceptive feedback [37], we hypothesize that the motor circuit controls ω, decreasing it in response to increasing external viscosity [16]. Consequently, k is either fixed spontaneously through mechanics or as a result of mechanical entrainment of coupled motor neuron oscillations [38]. We hypothesize that gait adaptation is *mechanically* enforced through the dispersion relation implied by the overall force balance. This mechanically regulated gait adaption helps to maintain a relatively constant overall speed across different environments [16]. Higher wave-number gaits produce higher kinematic efficiencies (larger displacements per cycle of undulation) [14], which compensate for the reduction in undulation frequency as viscosity is increased.

Finally, it is intriguing to consider our experimental results and the active beam model within the broader context of so-called "active solids" [39–41]. The systems studied in this work, namely, sinusoidally driven, overdamped, viscoelastic beams, freely moving in a fluid, represent an interesting subclass of active solids. We see that they display rich and counterintuitive dynamics. Understanding undulators as instances of a generic class of active solids may lead to insights into the behavior of a large number of related neuromechanical, cellular, subcellular, and even robotic [22] or synthetic active particle systems [42]. Moreover, because of their intrinsically wavelike dynamics, active undulators lend themselves to the use of conceptual and mathematical tools deployed in other wave systems in physics, such as dispersion relations. We hope that these findings will stimulate future experimental and theoretical use of dispersion relations to classify and understand the dynamics of active systems more broadly.

ACKNOWLEDGMENTS

This work was supported by NIH Grant No. R01AG082039, NSF Physics of Living Systems Student Research Network (Grant No. GR10003305), NSF-Simons Southeast Center for Mathematics and Biology (SCMB) through the National Science Foundation Grant No. DMS1764406 and Simons Foundation/SFARI Grant No. 594594. We would like to thank Professor Andrew Zangwill for useful discussions.

APPENDIX: APPLYING BOUNDARY CONDITIONS TO THE GENERAL CASE

For an unrestricted undulator, the appropriate boundary conditions are that the internal moments and forces go to zero at the spatial boundary points. In terms of the nondimensional lateral displacement $\upsilon(\sigma, \tau)$, the boundary conditions are given by Eqs. (12) and (15). Our first approach to solving this boundary-value problem is to substitute a right-traveling plane-wave ansatz into the nondimensional Eq. (3), and simplify to get the general dispersion relationship

$$k^4 - i\omega k^4 - e^{-i\phi}k^2 = \left(\frac{x_c}{x_\eta}\right)^4 (i\omega).$$

This (complex) polynomial is fourth order in k; we expect four roots when we solve for k. In the solutions that follow, we have abbreviated $a = x_c/x_\eta$.

$$\pm k_p = \pm\sqrt{\frac{e^{-i\phi} + \sqrt{e^{-2i\phi} + 4a^4\omega(i+\omega)}}{2(1-i\omega)}}, \tag{A1}$$

$$\pm k_m = \pm\sqrt{\frac{e^{-i\phi} - \sqrt{e^{-2i\phi} + 4a^4\omega(i+\omega)}}{2(1-i\omega)}}. \tag{A2}$$

Notice that the right-traveling plane-wave ansatz is separable. We surmise that a separable solution to the PDE (3) is given by

$$\begin{aligned} &\upsilon_{particular}(\sigma, \tau) \\ &\quad = e^{-i\omega\tau}[Ae^{-ik_m\sigma} + Be^{ik_m\sigma} + Ce^{-ik_p\sigma} + De^{ik_p\sigma}], \end{aligned}$$

with A, B, C, D denoting real coefficients that are to be determined. Next, we impose boundary conditions on this particular solution.

The boundary conditions, Eqs. (12) and (15), enforced at positions $\sigma = 0$ and $\sigma = L/x_c$ result in four linear equations in the coefficients, which we gather into a matrix equation

$$\mathbf{M}\begin{pmatrix} A \\ B \\ C \\ D \end{pmatrix} = \begin{pmatrix} 0 \\ 0 \\ 0 \\ 0 \end{pmatrix}. \tag{A3}$$

Here $\mathbf{M}$ is a 4×4 matrix that depends on ω, k, a, and ϕ, and each row of $\mathbf{M}$ corresponds with one of the four boundary conditions. It will not be necessary to write out $\mathbf{M}$ in full, because we can compute the null space indirectly.

If the matrix $\mathbf{M}$ is singular, there exist values of A, B, C, and D, not all zero, that satisfy Eq. (A3); these coefficients give nontrivial solutions to the equation of motion that also satisfy the boundary conditions. A matrix is singular if its determinant is zero:

$$\det \mathbf{M} = 0. \tag{A4}$$

By solving for the values of ω that make the determinant of $\mathbf{M}$ go to zero, we can identify the restrictions on the solutions imposed by the boundary conditions. We find that the following values of ω satisfy (A4):

$$\omega = -i \pm \sqrt{\frac{2}{a^4}}e^{-i\phi}, \tag{A5}$$

$$= \pm\sqrt{\frac{2}{a^4}}\cos\phi - i\left(1 \pm \sqrt{\frac{2}{a^4}}\sin\phi\right). \tag{A6}$$

Hence, in the case where both dissipation terms are included, the effect of the boundary does not introduce a length dependence, but does constrain the relationship between a, ϕ, and ω.

[1] E. M. Purcell, Life at low Reynolds number, Am. J. Phys. **45**, 3 (1977).

[2] D. L. Hu, J. Nirody, T. Scott, and M. J. Shelley, The mechanics of slithering locomotion, Proc. Natl. Acad. Sci. USA **106**, 10081 (2009).

[3] B. Chong, J. He, S. Li, E. Erickson, K. Diaz, T. Wang, D. Soto, and D. I. Goldman, Self-propulsion via slipping: Frictional swimming in multilegged locomotors, Proc. Natl. Acad. Sci. USA **120**, e2213698120 (2023).

[4] J. M. Rieser, B. Chong, C. Gong, H. C. Astley, P. E. Schiebel, K. Diaz, C. J. Pierce, H. Lu, R. L. Hatton, H. Choset, and D. I. Goldman, Geometric phase predicts locomotion performance in undulating living systems across scales, Proc. Natl. Acad. Sci. USA **121**, e2320517121 (2019).

[5] E. Lauga and T. R. Powers, The hydrodynamics of swimming microorganisms, Rep. Prog. Phys. **72**, 096601 (2009).

[6] Similar principles, often in the form of relationships between gait parameters, have been previously identified in many different categories of locomotion, including bipedal, quadrupedal, hexapodal, and myriapodal locomotion [43–46], flight [47], and aquatic swimming [48,49].

[7] J. Gray and G. Hancock, The propulsion of sea-urchin spermatozoa, J. Exp. Biol. **32**, 802 (1955).

[8] T. Zhang and D. I. Goldman, The effectiveness of resistive force theory in granular locomotion, Phys. Fluids **26**, 101308 (2014).

[9] G. K. Batchelor, Slender-body theory for particles of arbitrary cross-section in Stokes flow, J. Fluid Mech. **44**, 419 (1970).

[10] A. Shapere and F. Wilczek, Geometry of self-propulsion at low Reynolds number, J. Fluid Mech. **198**, 557 (1989).

[11] P. E. Schiebel, H. C. Astley, J. M. Rieser, S. Agarwal, C. Hubicki, A. M. Hubbard, K. Diaz, J. R. Mendelson, Iii, K. Kamrin, and D. I. Goldman, Mitigating memory effects during undulatory locomotion on hysteretic materials, eLife **9**, e51412 (2020).

[12] T. McMillen, T. Williams, and P. Holmes, Nonlinear muscles, passive viscoelasticity and body taper conspire to create neuromechanical phase lags in anguilliform swimmers, PLoS Comput. Biol. **4**, e1000157 (2008).

[13] Y. Ding, S. S. Sharpe, K. Wiesenfeld, and D. I. Goldman, Emergence of the advancing neuromechanical phase in a resistive force dominated medium, Proc. Natl. Acad. Sci. USA **110**, 10123 (2013).

[14] C. J. Pierce, Y. Ding, L. Peng, X. Lu, B. Chong, H. Lu, and D. I. Goldman, Neuromechanical phase lags and gait adaptation in the nematode *C. elegans*, PRX Life **3**, 023001 (2025).

[15] V. J. Butler, R. Branicky, E. Yemini, J. F. Liewald, A. Gottschalk, R. A. Kerr, D. B. Chklovskii, and W. R. Schafer, A consistent muscle activation strategy underlies crawling and swimming in Caenorhabditis elegans, J. R. Soc. Interface. **12**, 20140963 (2015).

[16] C. Fang-Yen, M. Wyart, J. Xie, R. Kawai, T. Kodger, S. Chen, Q. Wen, and A. D. Samuel, Biomechanical analysis of gait adaptation in the nematode Caenorhabditis elegans, Proc. Natl. Acad. Sci. USA **107**, 20323 (2010).

[17] See Supplemental Material at http://link.aps.org/supplemental/10.1103/lszs-51bf for experimental methods, a detailed derivation of the physical model and nondimensionalization scheme, as well as full page plots of the primary data in Figs. 2 and 4.

[18] M.-A. Félix and C. Braendle, The natural history of *Caenorhabditis elegans*, Curr. Biol. **20**, R965 (2010).

[19] G. Juarez, K. Lu, J. Sznitman, and P. E. Arratia, Motility of small nematodes in wet granular media, Europhys. Lett. **92**, 44002 (2010).

[20] X. Shen and P. E. Arratia, Undulatory swimming in viscoelastic fluids, Phys. Rev. Lett. **106**, 208101 (2011).

[21] T. Majmudar, E. E. Keaveny, J. Zhang, and M. J. Shelley, Experiments and theory of undulatory locomotion in a simple structured medium, J. R. Soc. Interface **9**, 1809 (2012).

[22] T. Wang, C. Pierce, V. Kojouharov, B. Chong, K. Diaz, H. Lu, and D. I. Goldman, Mechanical intelligence simplifies control in terrestrial limbless locomotion, Sci. Robot. **8**, eadi2243 (2023).

[23] To avoid confusion, we use the following notational convention throughout the manuscript. For dimensionless quantities, we use the angular frequency and wave number ω and k. When presenting experimental data, we use the corresponding linear frequency and inverse wavelength in SI units, denoted f and $1/\lambda$, respectively.

[24] Z. V. Guo and L. Mahadevan, Limbless undulatory propulsion on land, Proc. Natl. Acad. Sci. USA **105**, 3179 (2008).

[25] In the small-amplitude limit used in this manuscript, the normal fluid drag is approximated by $C\frac{\partial y}{\partial t}$ and the y component of the tangential fluid drag is negligible.

[26] T. McMillen and P. Holmes, An elastic rod model for anguilliform swimming, J. Math. Biol. **53**, 843 (2006).

[27] J.. Cheng, T. J. Pedley, and J. D. Altringham, A continuous dynamic beam model for swimming fish, Philos. Trans. R. Soc. Lond. B Biol. Sci. **353**, 981 (1998).

[28] The full equation of motion and both limiting cases produce the same wave-stability criterion.

[29] J. F. van Weerden, D. A. P. Reid, and C. K. Hemelrijk, A meta-analysis of steady undulatory swimming, Fish Fish. **15**, 397 (2014).

[30] M. F. Velho Rodrigues, M. Lisicki, and E. Lauga, The bank of swimming organisms at the micron scale (BOSO-Micro), PLoS One **16**, e0252291 (2021).

[31] J. Gray and H. W. Lissmann, The locomotion of nematodes, J. Exp. Biol. **41**, 135 (1964).

[32] K. M. Dorgan, C. J. Law, and G. W. Rouse, Meandering worms: Mechanics of undulatory burrowing in muds, Proc. Biol. Sci. USA **280**, 20122948 (2013).

[33] J. Maes, L. Verlooy, O. E. Buenafe, P. A. M. de Witte, C. V. Esguerra, and A. D. Crawford, Evaluation of 14 organic solvents and carriers for screening applications in Zebrafish embryos and larvae, PLoS ONE **7**, e43850 (2012).

[34] V. Fischbach, A. Finke, T. Moritz, P. Polte, and P. Thieme, A staging system for Atlantic herring (*Clupea harengus*) larvae based on external morphology and skeletal development, Limnol. Oceanogr. Methods **21**, 357 (2023).

[35] R. Rikmenspoel, The equation of motion for sperm flagella, Biophys. J. **23**, 177 (1978).

[36] R. L. Panton, *Incompressible Flow*, 5th ed. (Wiley, Somerset, NJ, 2024).

[37] H. Ji, A. D. Fouad, S. Teng, A. Liu, P. Alvarez-Illera, B. Yao, Z. Li, and C. Fang-Yen, Phase response analyses support a relaxation oscillator model of locomotor rhythm generation in Caenorhabditis elegans, eLife **10**, e69905 (2021).

[38] C. L. Johnson, T. J. Lewis, and R. Guy, Neuromechanical mechanisms of gait adaptation in *C. elegans*: Relative roles of neural

and mechanical coupling, SIAM J. Appl. Dyn. Syst. **20**, 1022 (2021).

[39] E. Ferrante, A. E. Turgut, M. Dorigo, and C. Huepe, Collective motion dynamics of active solids and active crystals, New J. Phys. **15**, 095011 (2013).

[40] A. Shee, S. Henkes, and C. Huepe, Emergent mesoscale correlations in active solids with noisy chiral dynamics, Soft Matter **20**, 7865 (2024).

[41] J. Veenstra, C. Scheibner, M. Brandenbourger, J. Binysh, A. Souslov, V. Vitelli, and C. Coulais, Adaptive locomotion of active solids, Nature (London) **639**, 935 (2025).

[42] Q. Martinet, Y. I. Li, A. Aubret, E. Hannezo, and J. Palacci, Emergent dynamics of active elastic microbeams, Phys. Rev. X **15**, 041017 (2025).

[43] N. C. Heglund, C. R. Taylor, and T. A. McMahon, Scaling stride frequency and gait to animal size: Mice to horses, Science **186**, 1112 (1974).

[44] M. Hildebrand, The quadrupedal gaits of vertebrates: The timing of leg movements relates to balance, body shape, agility, speed, and energy expenditure, Biosci. **39**, 766 (1989).

[45] R. J. Full and M. S. Tu, Mechanics of a rapid running insect: Two-, four- and six-legged locomotion, J. Exp. Biol. **156**, 215 (1991).

[46] B. Chong, J. He, D. Soto, T. Wang, D. Irvine, G. Blekherman, and D. I. Goldman, Multilegged matter transport: A framework for locomotion on noisy landscapes, Science **380**, 509 (2023).

[47] T. N. Sullivan, M. A. Meyers, and E. Arzt, Scaling of bird wings and feathers for efficient flight, Sci. Adv. **5**, eaat4269 (2019).

[48] M. Gazzola, M. Argentina, and L. Mahadevan, Scaling macroscopic aquatic locomotion, Nat. Phys. **10**, 758 (2014).

[49] J. Sánchez-Rodríguez, C. Raufaste, and M. Argentina, Scaling the tail beat frequency and swimming speed in underwater undulatory swimming, Nat. Commun. **14**, 5569 (2023).

Supplemental Material

EXPERIMENTAL METHODS

Worm Cultivation and Age Synchronization

C. elegans (strain N2) were cultivated on NGM plates seeded with *Escherichia coli* (strain OP50) at 20°C. Before experiments, worms were age synchronized by hatch off (Day 1 Adult), and starved for 1 hour on unseeded NGM plates.

Methylcellulose Solutions and Experiments

Methylcellulose solutions were prepared at 1%, 2%, and 3% percent by weight in an S-basal medium. The viscosity was calculated based on the provided reference value of 4000 cp for a 2% aqueous solution at 20°C. Worms were imaged in droplets placed between two glass slides, using a single coverslip (No. 1) as a spacer and imaged in brightfield using a dissecting scope (Leica).

Polyethelyne glycol Solutions and Experiments

To encapsulate synchronized adult worms in gels, we used a norborene-thiol photo-click method similar to [1]. We mixed equal parts of PEG-Th and PEG-NB to combined weight percents of 1-5% PEG by volume. These mixtures were aliquoted into small volumes ($10\mu L$) and frozen at -20°C. Before use in experiments, the samples were thawed and mixed with a UV-photo-initiator (LAP) at a wt-% of 0.5%. The liquids were then pipetted in small volumes ($2\mu L$) into a sample chamber made by cutting hydrophobic tape using a method similar to [2]. Worms were placed in the liquid phase PEG-LAP mixture using a worm pick and covered with a silicon oil droplet to prevent evaporation. Worms were recorded swimming for 5 minutes using an inverted microscope in bright-field mode (Nikon) at 5x magnification in the liquid phase medium and then exposed to a 1 second UV light pulse *in situ* from a solid state LumenCore Light Engine focused onto the sample plane. After the UV light was removed, the worms were imaged for an additional 5-minute interval in the gel phase medium.

Agar Plate Preparation and Experiments

NGM plates were poured into 6cm petri dishes and stored at 4°C before use in experiments. Plates were placed at room temperature for ∼2 hours prior to experiments. For behavior recordings, worms were imaged on the same plates they were starved on using a dissecting scope (Leica).

Image Analysis

Bouts of forward locomotion containing a minimum of three cycles of forward locomotion were isolated from the recordings. Centerlines were extracted from video recordings using a threshold-based method similar to [3]. Centerlines were splined using a B-spline method implemented in Matlab. From the spline curve, the curvature was calculated at each point along the body. To calculate the undulation frequency f, the time domain Fast Fourier Transform (FFT) of the curvature κ was calculated at a set of points along the body. The peak frequency at each body point was determined, and then averaged over all the body points. Because of the finite length of the worm, spectral methods such as FFT were unreliable to estimate the wavelength λ. Instead, we estimated the wave speed first, using spatial covariance matrices as detailed in [4]. We then divided the wavespeed by the undulation frequency to calculate λ.

MODEL DERIVATION

We begin by considering a driven viscoelastic beam immersed in a low Reynolds number fluid. Force balance transverse to the beam's long axis produces the following PDE, used previously by Fang-yen et al [3],

$$\frac{\partial^2}{\partial s^2}\left[b_e\kappa + b_\eta\dot{\kappa} + m\cdot h\right] = F_{\text{fluid}}, \tag{1}$$

where

- $b_e\kappa$ is the elastic body torque,
- $b_\eta\dot{\kappa}$ is the viscous body torque,

- $m \cdot h$ is the muscle torque as a function of position and time, and
- F_{fluid} is the fluid drag component transverse to the beam.

Furthermore, the units are as follows.

- The units on b_e are [force] $\cdot$ [length]^2. In SI units, $b_e \approx 9.5 * 10^{-14} [N \cdot m^2]$.
- The units on b_η are [force] $\cdot$ [length]^2 $\cdot$ [time]. In SI units, $b_\eta \approx 5 * 10^{-16} [N \cdot m^2 \cdot s]$.
- The constant C (below) has units of viscosity. In SI units, $C \approx 10^{-3} [N \cdot s/m^2]$ in buffer.
- The units of m are [force] $\cdot$ [length]. In SI units, $m \approx 10^{-9} [N \cdot m]$.

The estimated values of the parameters above were taken from [3].

A solution to the PDE (1) will be a function $\kappa(s, t)$ that gives the curvature of the viscoelastic beam at position s and at time t. Note that the variable s measures the position along the body length of the worm. See Fig. 1(a) below.

Following Fang-yen [3], we make three approximations that are shown in Fig. 1(a). We approximate the normal velocity by the velocity of the transverse displacement y such that

$$F_{\text{fluid}} = -C v_N \approx -C \frac{\partial y}{\partial t}, \tag{2}$$

where C is the transverse drag coefficient. We can re-write the left-hand side of equation (1) in terms of the transverse displacement y using the following approximation

$$\kappa \approx \frac{\partial^2 y}{\partial s^2} = y_{ss}, \tag{3}$$

where we have adopted the convention that independent variables as subscripts indicate partial differentiation: $\frac{\partial y}{\partial s} = y_s$.

Finally we make the approximation $s \approx x$, which is valid for small displacements y. Substituting these approximations into equation (1) leads to

$$b_e y_{xxxx} + b_\eta \frac{\partial}{\partial t} y_{xxxx} + m h_{xx} = -C \frac{\partial y}{\partial t}. \tag{4}$$

Here we have written the active muscle torque as $m \cdot h(x, t)$, where m is a constant with dimensions of torque, $N \cdot m$, and where h is a dimensionless function representing the muscle activity spatial and temporal variation as commanded by the locomotor circuit.

We proceed to nondimensionalize the equation (4) by making the substitutions $t = t_c\tau$, $x = x_c\sigma$, and $y = x_c\upsilon$, where t_c and x_c are characteristic time and length scales respectively, and τ, υ, and σ are the corresponding dimensionless variables. This yields

$$\frac{b_e}{x_c^3}\upsilon_{\sigma\sigma\sigma\sigma} + \frac{b_\eta}{t_c x_c^3}\dot{\upsilon}_{\sigma\sigma\sigma\sigma} + \frac{m}{x_c^2}h_{\sigma\sigma} = -\frac{C x_c}{t_c}\dot{\upsilon}. \tag{5}$$

As above, a variable in a subscript denotes partial differentiation. In this and in the following equations, an overdot denotes partial differentiation with respect to the variable τ. Next, we divide both sides of the above equation by the leading order coefficient $\frac{b_\eta}{t x_c^3}$, which gives

$$t_c\frac{b_e}{b_\eta}\upsilon_{\sigma\sigma\sigma\sigma} + \dot{\upsilon}_{\sigma\sigma\sigma\sigma} + x_c t_c\frac{m}{b_\eta}h_{\sigma\sigma} = -x_c^4\frac{C}{b_\eta}\dot{\upsilon}. \tag{6}$$

To obtain the dimensionless time, we set $t_c b_e/b_\eta = 1$ and substitute $t_c = b_\eta/b_e$, yielding

$$\upsilon_{\sigma\sigma\sigma\sigma} + \dot{\upsilon}_{\sigma\sigma\sigma\sigma} + x_c\frac{m}{b_e}h_{\sigma\sigma} = -x_c^4\frac{C}{b_\eta}\dot{\upsilon}. \tag{7}$$

From this expression, we see that there are two choices of a characteristic length scale in the problem, obtained by either setting $x_c m/b_e = 1$ or setting $x_c^4 C/b_\eta = 1$. We chose to nondimensionalize via the former length scale, which is discussed in the main text. We define the second characteristic length scale as $x_\eta = (b_\eta/C)^{1/4}$. The meaning of these length and time scales are discussed in the final section of this supplement.

After substituting, we finally arrive at a fully dimensionless PDE,

$$\upsilon_{\sigma\sigma\sigma\sigma} + \dot{\upsilon}_{\sigma\sigma\sigma\sigma} + h_{\sigma\sigma} = -\left(\frac{x_c}{x_\eta}\right)^4\dot{\upsilon}. \tag{8}$$

We further assume that the muscle force is a traveling wave that is phase-shifted, when compared to the body undulation, as described in the main text. This assumption allows us to substitute

$$h = e^{-i\phi}\cdot\upsilon. \tag{9}$$

We assume that $\phi > 0$ is small, and the phase shift is chosen to be $e^{-i\phi}$ so that the muscle oscillation occurs in advance of the body undulation, as observed in experiments comparing measured muscle activity and body bending patterns [4–6].

SOLVING THE EQUATION OF MOTION

We now begin the task of solving the fifth-order PDE (8) with the particular choice of muscle term $h = e^{-i\phi} \cdot \upsilon$. The reader can easily check that a right-traveling complex plane wave ansatz,

$$\upsilon(\sigma, \tau) = \exp(i(k\sigma - \omega\tau)),$$

is a solution to the PDE provided that the following relationship is satisfied

$$k^4 - e^{-i\phi}k^2 = i\omega \cdot ((x_c/x_\eta)^4 + k^4).$$

This is equivalent to

$$\omega = \frac{ik^2(e^{-i\phi} - k^2)}{(x_c/x_\eta)^4 + k^4} = \underbrace{\frac{k^2 \sin(\phi)}{(x_c/x_\eta)^4 + k^4}}_{\text{real part}} + i \cdot \underbrace{\frac{k^2 \cos(\phi) - k^4}{(x_c/x_\eta)^4 + k^4}}_{\text{imaginary part}}.$$

We call this result the dispersion relation. We could, instead, solve for k as a function of ω, which is done in Appendix I of the main text.

VISUALIZING THE k AND ω DEPENDENCE OF THE FORCES

The existence of the two scaling regimes described by the simplfied PDEs in the previous section reflect the different k and ω dependence of the various force terms (muscle force, internal dissipation, and fluid drag), which in turn reflect the order of the spatial and temporal derivatives. Figure 1 illustrates the k and ω dependence of the force terms that determine the overall scaling of the real part of the dispersion relation. For example the balance of external fluid drag and muscle forces (visualized by the intersection of the blue and red surfaces) defines a curve where $\omega \propto k^2$. In contrast, the balance of the internal dissipation and the muscle forces (visualized by the intersection of the green and red surfaces) defines a curve where $\omega \propto k^{-2}$. The presence of *both* dissipative terms produces a curve that smoothly interpolates between these two regimes [Fig. 1(b), dashed curve], provided the stability criterion is satisfied over the appropriate range of wavenumber k.

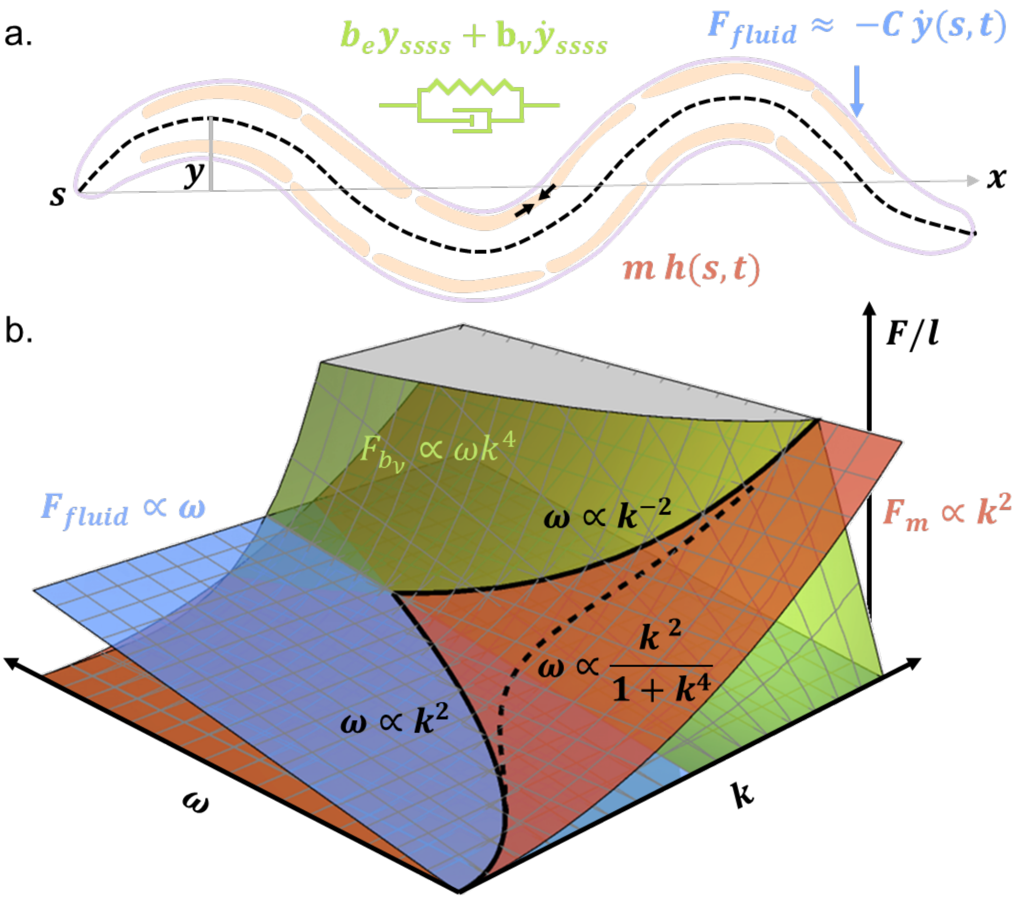

FIG. 1. (a) schematic illustration of the model, reproduced from the main document. b) the k and ω dependence of the various force terms contributing to the scaling of the dispersion relation. In this illustration x_c/x_η =1 and wave stability is not considered.

PHYSICAL INTERPRETATION OF t_c, x_c, AND x_η

Having described the role of the various parameters in the model in selecting a particular scaling regime and frequency scale, we proceed to discuss the physical meaning of x_η, x_e and t_c.

We first consider the time scale, t_c, which is the viscoelastic time constant. If we consider a worm without muscle forcing or external drag, equation (1) reduces to

$$b_e \kappa = -b_\eta \dot{\kappa} \tag{10}$$

which has solutions

$$\kappa(t) = \kappa_0 e^{-\frac{b_e}{b_\eta}t} = \kappa_0 e^{-\frac{t}{t_c}} \tag{11}$$

Hence, t_c may be interpreted as the decay constant of a worm bent to some initial curvature κ_0 and allowed to relax under the viscoelastic torques from within the body.

Next, we consider the elastic length-scale $x_c = b_e/m$. If we ignore the effect of viscous forces, and consider a constant muscle torque (i.e. $h(x,t) = 1$) applied to the body, the equation of the muscle torque and the body elastic torque

$$m = b_e \kappa \tag{12}$$

implies that elastic length scale is the maximum radius of curvature achievable body muscle torque of magnitude m

$$1/\kappa = r_{max} = \frac{b_e}{m} = x_c \tag{13}$$

Put another way, a constant muscle torque m, at steady state (after viscous responses stop) would produce a bend with a radius of curvature of x_c.

Finally, we consider the viscous length-scale $x_\eta = (b_\eta/C)^{1/4}$. To understand the physical meaning of this seemingly counterintuitive length scale, we consider the viscous body force $b_\eta \frac{\partial}{\partial t} y_{xxxx}$ and the external fluid torque $-C\dot{y}$ from Eqn. 4 for an undulator oscillating with the following traveling wave solution

$$y(x,t) = y_0 \sin(2\pi(x/\lambda - ft)) \tag{14}$$

Because the body viscous force contains 4 spatial derivatives (and a single time derivatve), it will depend on the wavelength (and frequency) as follows

$$F_{b_\eta} = -(2\pi)^5 y_0 \; b_\eta \frac{f}{\lambda^4} \cos(2\pi(x/\lambda - ft)) \tag{15}$$

The transverse component of the viscous fluid drag F_{fluid}, having no spatial derivatives (and a single time derivatve), will be independent of λ:

$$F_{\text{fluid}} = -2\pi C f \cos(2\pi(x/\lambda - ft)). \tag{16}$$

Setting the two fluid drags equal to one another, we find that

$$\frac{2\pi}{\lambda} = \left(\frac{C}{b_\eta}\right)^{1/4} = \frac{2\pi}{x_\eta}\,. \tag{17}$$

This implies that x_η is the wavelength at which the body viscous drag and external fluid drag are equal. As discussed above and in the main text, this is the sole parameter that determines which scaling regime a given undulator will obey (either $\omega \propto k^2$ or $\omega \propto k^{-2}$).

BIBLIOGRAPHY

[1] C.-C. Lin, C. S. Ki, and H. Shih, J. Appl. Polym. Sci. **132** (2015).

[2] G. Sun, C.-A. Manning, G. H. Lee, M. Majeed, and H. Lu, Adv. Healthc. Mater. **10**, e2001887 (2021).

[3] C. Fang-Yen, M. Wyart, J. Xie, R. Kawai, T. Kodger, S. Chen, Q. Wen, and A. D. Samuel, Proceedings of the National Academy of Sciences **107**, 20323 (2010).

[4] C. J. Pierce, Y. Ding, B. Chong, H. Lu, and D. I. Goldman, bioRxiv , 2024.05.06.592744 (2024).

[5] T. McMillen, T. Williams, and P. Holmes, PLoS computational biology **4**, e1000157 (2008).

[6] Y. Ding, S. S. Sharpe, K. Wiesenfeld, and D. I. Goldman, Proceedings of the National Academy of Sciences **110**, 10123 (2013).

DATA WITH LEGEND

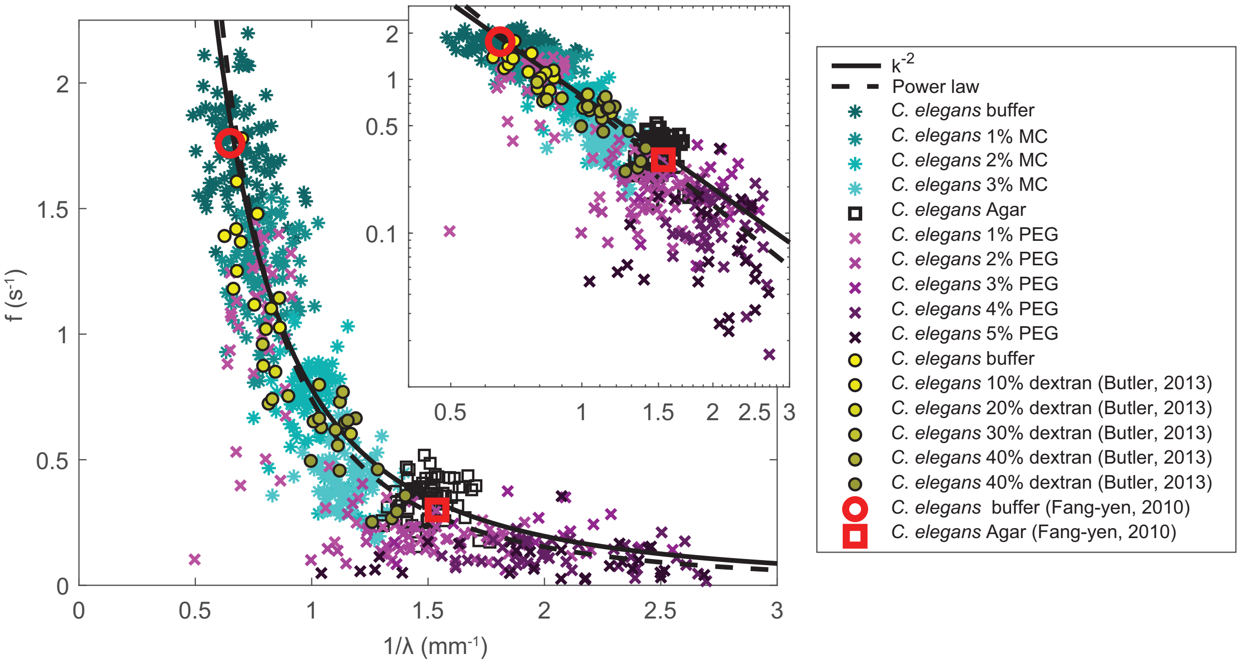

FIG. 2. Worm data across environments in linear and log-log scaling.

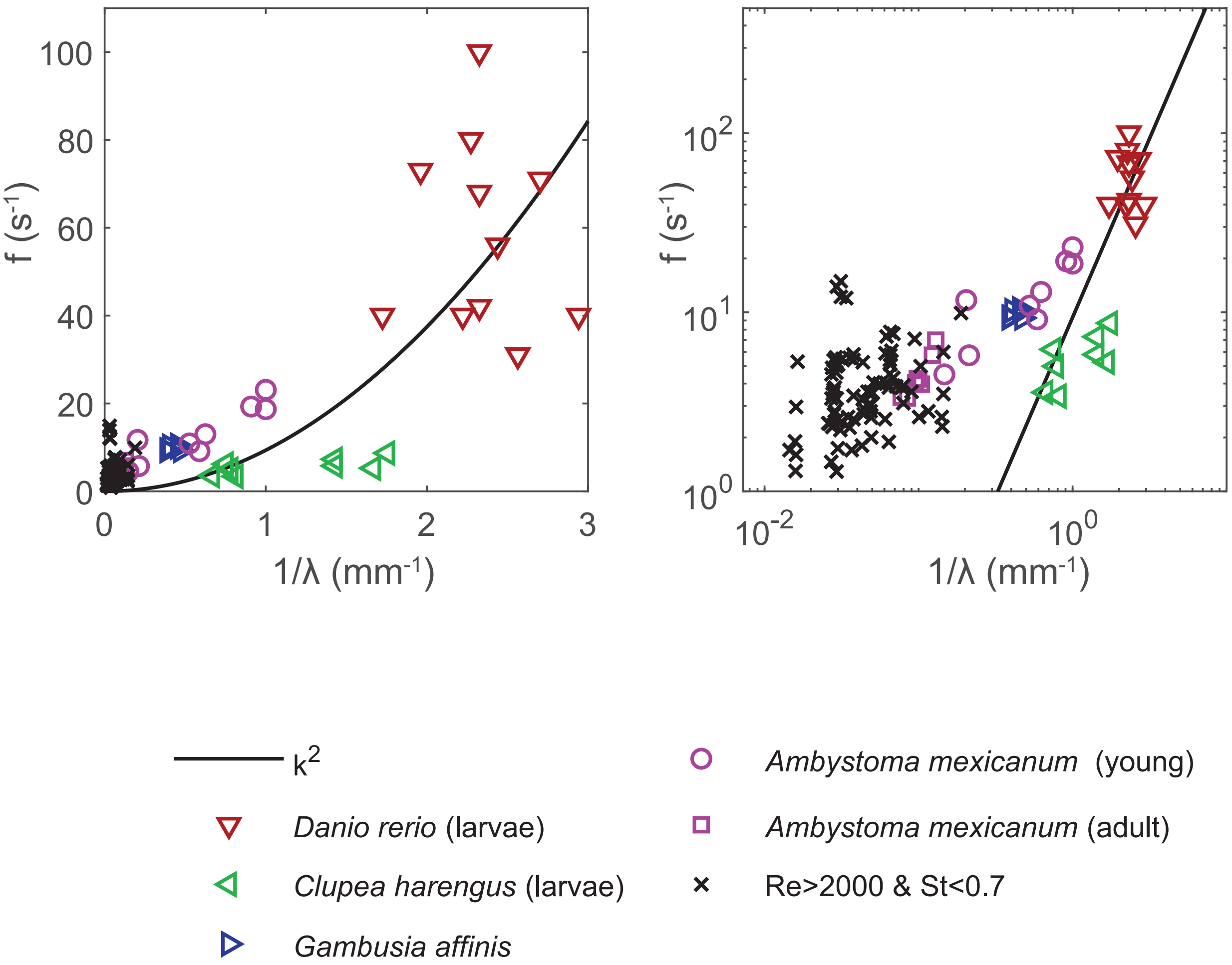

FIG. 3. Fish data in linear (left) and log-log scaling (right).

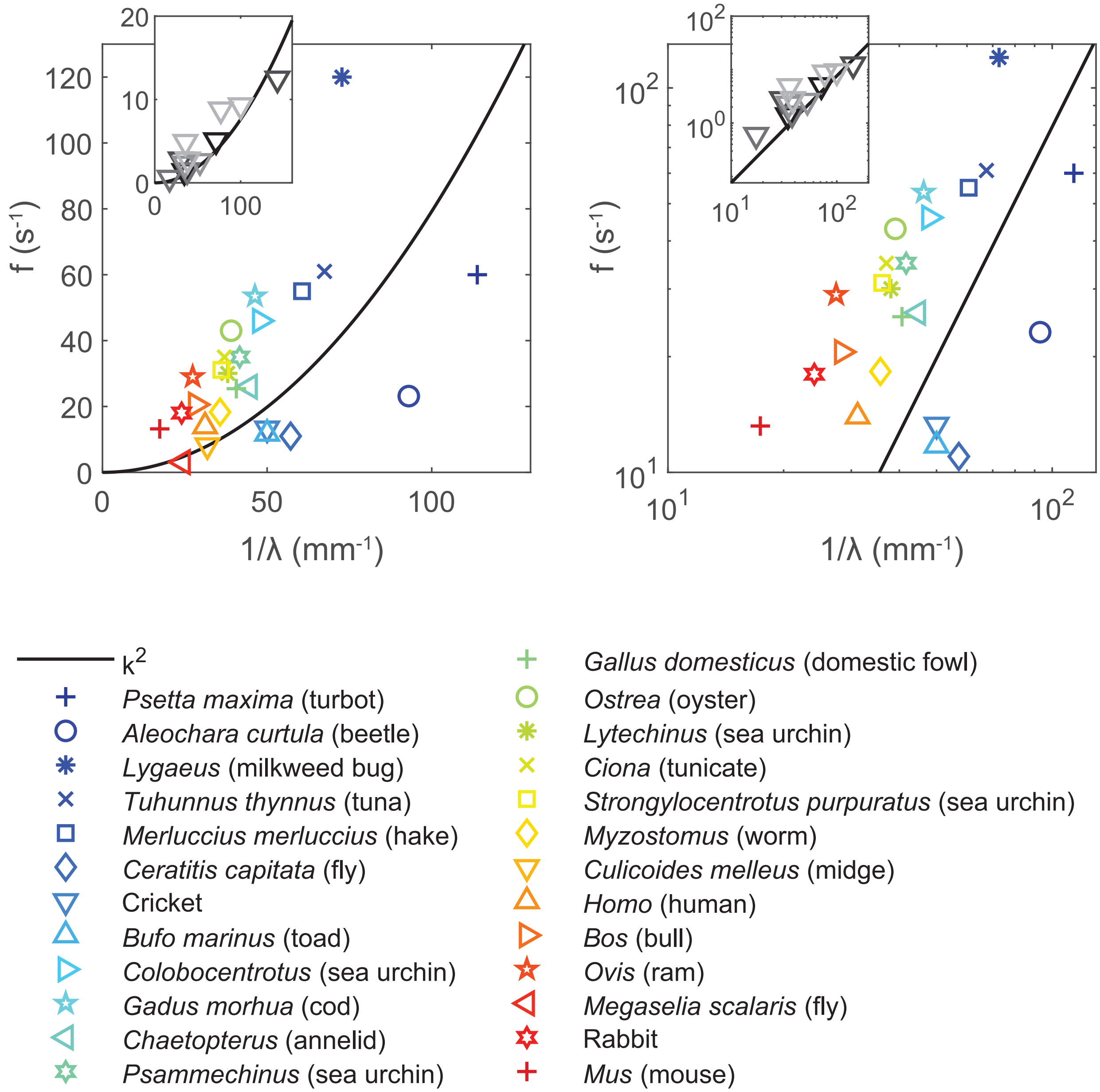

FIG. 4. Spermatozoa data in linear (left) and log-log scaling (right). Inset in both figures shows individual cricket data